7-2021

Scaling of oscillatory kinematics and Froude efficiency in baleen whales

William T. Gough

Hayden J. Smith

Matthew S. Savoca

Max F. Czapanskiy

Frank E. Fish

See next page for additional authors

Authors

William T. Gough, Hayden J. Smith, Matthew S. Savoca, Max F. Czapanskiy, Frank E. Fish, Jean Potvin, K. C. Bierlich, David E. Cade, Jacopo Di Clemente, John Kennedy, Paolo Segre, Andrew Stanworth, Caroline Weir, and Jeremy A. Goldbogen

Scaling of oscillatory kinematics and Froude efficiency in baleen whales

*William T. Gough[1], Hayden J. Smith[1,2], Matthew S. Savoca[1], Max F. Czapanskiy[1], Frank E. Fish[3], Jean Potvin[4], K.C. Bierlich[5], David E. Cade[1,6], Jacopo Di Clemente[7], John Kennedy[4], Paolo Segre[1], Andrew Stanworth[8], Caroline Weir[8], Jeremy A. Goldbogen[1]

[1]Hopkins Marine Station, Stanford University, Pacific Grove, CA, [2]Southwestern University, Georgetown, TX, [3]West Chester University, West Chester, PA, [4]Saint Louis University, Saint Louis, MO, [5]Duke University, Durham, NC, [6]University of California Santa Cruz, Santa Cruz, CA, [7]Department of Biology, University of Copenhagen, Copenhagen, Denmark, [8]Falklands Conservation, Stanley, Falkland Islands

*Corresponding Author

Key Words

Cetacean, Swimming, Hydrodynamics, Thrust, Efficiency

Summary Statement

We used tags attached to baleen whales to demonstrate how thrust power output, drag coefficient, and Froude efficiency scale with swimming speed and body length.

Abstract

High efficiency lunate-tail swimming with high-aspect-ratio lifting surfaces has evolved in many vertebrate lineages, from fish to cetaceans. Baleen whales (Mysticeti) are the largest swimming animals that exhibit this locomotor strategy and present an ideal study system to examine how morphology and the kinematics of swimming scale to the largest body sizes. We used data from whale-borne inertial sensors coupled with morphometric measurements from aerial drones to calculate the hydrodynamic performance of oscillatory swimming in six baleen whale species ranging in body length from 5-25m (fin whale, *Balaenoptera physalus*; Bryde's whale, *Balaenoptera* edeni; sei whale, *Balaenoptera* borealis; Antarctic minke whales, *Balaenoptera bonaerensis*; humpback whales, *Megaptera novaeangliae*; and blue whales, *Balaenoptera musculus*). We find that mass-specific thrust increases with both swimming speed and body size. Froude efficiency, defined as the ratio of useful power output to the rate of energy input (Sloop, 1978), generally increased with swimming speed but decreased on average with increasing body size. This finding is contrary to previous results in smaller animals where Froude efficiency increased with body size. Although our empirically-parameterized estimates for swimming baleen whale drag was higher than that of a simple gliding model, oscillatory locomotion at this scale exhibits generally high Froude efficiency as in other adept swimmers. Our results quantify the fine-scale kinematics and estimate the hydrodynamics of routine and energetically expensive swimming modes at the largest scale.

Introduction

The repeated invasion of aquatic and marine environments by tetrapods over the last 250 million years has resulted in a host of convergent morphological adaptations that facilitate life in water (Kelley & Pyenson, 2015). Among these adaptations are the evolution of a fusiform body shape, flattened control surfaces, and sickle-shaped caudal fin to achieve high performance locomotion (Fish et al., 2008). These morphological adaptations are functionally analogous among swimming animals such as thunniform fish, lamnid sharks, cetaceans, and the extinct ichthyosaurs (Motani, 2002; Donley et al., 2004; Gleiss et al., 2011). The majority of these swimmers use an oscillatory swimming style that involves side-to-side or up-and-down movement of a hydrofoil-like tail to generate lift-based thrust and overcome drag (Fish, 1998). Cetaceans are unique among oscillatory swimmers because of their extreme body mass, exemplified in modern baleen whales (Mysticeti), which evolved massive body sizes within the last five million years (Slater et al., 2017).

Although the swimming performance of large whales has long been of interest to researchers (Krogh, 1934; Kermack, 1948; Bose & Lien, 1989), direct measures of their swimming kinematics and morphology have been difficult to obtain. Studies of cetacean swimming kinematics have typically focused on smaller and highly maneuverable odontocete species in captivity (Fish, 1993; Curren et al., 1994; Fish, 1998, Fish et al, 2014). Attempts to study mysticetes and derive energetic assumptions (Sumich, 1983; Parry, 1949; Blix & Folkow, 1995) were constrained to breathing events at the water's surface, and morphological measurements were only attainable from deceased animals that had stranded on beaches or been captured by whaling operations (Lockyer, 1976; Kahane-Rapport & Goldbogen, 2018). The

recent development of high-resolution biologging methods now allows researchers to quantify the kinematics of free-swimming cetaceans in their natural habitats (Johnson & Tyack, 2003; Goldbogen et al., 2017a; Gough et al., 2019). In addition, unoccupied aircraft systems (UAS, or drone) technology has enhanced our ability to obtain precise morphological data, thereby enabling comparative and scaling analyses of form and function (Gough et al., 2019; Christiansen et al., 2019; Kahane-Rapport et al., 2020).

Understanding the size-dependent kinematics of swimming cetaceans is critical to analyze their swimming performance and energetics. The dorso-ventral oscillation of the flukes produces lift that is resolved into a forward thrust vector (Fig. 1; Lighthill, 1971; Chopra & Kambe, 1977; Vogel, 1994; Fish, 1998). This lift-based thrust power is equal to the drag power of the animal when swimming at a constant velocity (Lighthill, 1971; Fish, 1998). This mechanism is considered to be highly efficient (>75%; Triantafyllou et al., 1991; Rohr & Fish, 2004). Previous attempts to estimate the thrust power of actively swimming large whales have been made based on a number of assumptions without reliable kinematic data (Parry, 1949; Chopra & Kambe, 1977; Yates, 1983; Bose & Lien, 1989). Thrust power generation is modulated through the adjustment of basic kinematic parameters of the oscillatory tailbeat cycle, and new biologging tags make these empirical measurements possible for large, free-swimming animals.

Kinematic studies performed on cetaceans have focused on the three fundamental parameters of an oscillatory tailbeat cycle: amplitude of heave, swimming speed, and oscillatory frequency. Among these, speed has been studied most extensively. Using various methods, researchers have found that many different species of cetaceans are able to swim over an extended range of speeds. High speeds in excess of 8 m/s have been achieved by rorqual

mysticetes (Fish & Rohr, 1999; Hirt et al., 2017; Segre et al., 2020). A recent study by Gough et al. (2019) has shown that mysticetes tend to swim at ~2 m/s when not feeding. In order to swim at different speeds within this wide range, mysticetes must adjust either their oscillatory frequency or the amplitude of heave (Lighthill, 1971; Chopra & Kambe, 1977). For small odontocetes, Fish (1998) found that oscillatory frequency increased with increasing swimming speed but decreased roughly with body length while amplitude of heave remained constant at ~0.2 of an animal's body length. These findings were recently confirmed for mysticetes by Gough et al. (2019).

Measuring the fundamental kinematic parameters of the oscillatory tailbeat cycle has allowed researchers to estimate Froude efficiency, or the percentage of thrust that is successfully transferred into forward motion (Vogel, 1994; Fish, 1998). The dimensionless Strouhal number has typically been used as a rough way to describe how the amplitude of heave, swimming speed, and oscillatory frequency are modulated and interact to provide a maximally efficient pattern of vorticity around the tail during swimming (Triantafyllou et al., 1991; Fish, 1998; Taylor et al., 2003; Rohr & Fish, 2004; Gough et al., 2019). The generally accepted rule is that highly-efficient oscillatory swimming falls within a Strouhal range from 0.25-0.35 (Triantafyllou et al., 1991). Both Rohr & Fish (2004) and Gough et al. (2019) found that cetaceans fall within this range, but a more detailed analysis of the kinematics and hydrodynamic parameters, such as the thrust power output and drag, has only been performed previously by Fish (1998) for much smaller odontocetes.

Here, our goal is to move beyond the Strouhal number and use a combination of whale-borne tags and UAS morphological measurements to calculate the kinematics, thrust power output, and Froude efficiencies for free-swimming mysticete whales using methods similar to Fish (1998). Apart from Gough et al. (2019), we have a very limited understanding of how kinematics affect swimming performance at the upper extremes of body size. Previous studies have estimated the Froude efficiency of swimming for odontocetes and other oscillatory swimming animals to be approximately ~75-90% (Fish, 1998), but the only estimate for a mysticete prior to our study came from a single fin whale (*Balaenoptera physalus*) of unknown body size swimming at ~8 m/s (Bose & Lien, 1989). Our current data set goes beyond any previous analyses and includes six species and a ~5x range in body length. All of the species included in our study are lunge feeders which open their mouth wide prior to engulfing a large volume of water into a highly expansible throat pouch (Goldbogen et al., 2017b). This behavior requires the efficient achievement of high swimming speeds in order to maintain a favorable energetic balance (Potvin et al., 2009; 2020; 2021). We hypothesize that the kinematic and hydrodynamic parameters of swimming scale similarly between small and large cetaceans and will lead to high (>75%) Froude efficiencies for even the largest animals. Our study will lead to a more complete scaling-based understanding of oscillatory swimming in mysticetes and the kinematic, hydrodynamic, and morphological factors that impact swimming performance in the world's largest animals.

Methods

Study species and locations

The whales included in this study are the Antarctic minke whale (*Balaenoptera bonaerensis*, Burmeister, 1867), humpback whale (*Megaptera novaeangliae*, Borowski, 1781), fin whale (*Balaenoptera physalus*, Linnaeus, 1758), Bryde's whale (*Balaenoptera* edeni, Anderson, 1879), sei whale (*Balaenoptera borealis*, Lesson, 1828), and blue whale (*Balaenoptera musculus*, Linnaeus, 1758). The six species are members of the family Baleanoptera, commonly referred to as rorquals, and tend to have similar life histories and behaviors. These species range in size from ~5 m in length for the Antarctic minke whale up to ~25 m for an adult blue whale (Goldbogen et al., 2019). Distinct morphological differences are also present between these species (Kahane-Rapport & Goldbogen, 2018), with the most prominent being the enlarged flukes and flippers of the humpback whale relative to body size (Fish & Battle, 1995; Woodward et al., 2006).

Data on foraging and swimming was collected on humpback whales off of the coast of Monterey, CA and the Western Antarctic Peninsula, blue whales off California (Monterey Bay and Southern California Bight), Antarctic minke whales off the western Antarctic Peninsula, fin whales in Monterey Bay and the fjords of southeastern Greenland, Bryde's whales off the southern coast of South Africa, and sei whales near the Falkland Islands. All work was performed under suitable permits and in accordance with university IACUC procedures (See Acknowledgements section below).

CATS Tags

The Customized Animal Tracking Solutions (CATS) tags integrate video with 400 Hz accelerometers and gyroscopes; 50 Hz magnetometers, pressure and temperature sensors; a 10 Hz internal temperature sensor; and 10 Hz light and GPS sensors. Tag accelerometers for all whales were sampled at 40 or 400 Hz, magnetometers and gyroscopes at 40 or 50 Hz, and pressure, light, temperature, and GPS at 10 Hz. All data were decimated to 10 Hz, tag orientation on the animal was corrected for, and animal orientation was calculated using custom-written scripts in Matlab 2014a (following Johnson & Tyack, 2003; Cade et al., 2016). Animal speed for all deployments was determined using the amplitude of tag vibrations, a method which has been shown to be robust and accurate above ~ 1 m s^{-1} in a variety of behavioral contexts (Cade et al., 2018). The tags were deployed from rigid-hull inflatable boats using a 6 m carbon-fiber pole. These attached to the animal via four suction cups, detached after suction failed, floated to the surface and recovered via VHF telemetry. Deployment lengths in this study ranged from 8 mins to 26 hrs. For more information on the type of tag used in this study, see Goldbogen et al. (2017a).

UAS Operations and *Morphometric Measurements*

Images of each species were collected using UAS between 2017 and 2019. Specifically, two types of stock-build quadcopters, the Phantom 3 and Phantom 4 Pro, as well as two types of custom hexacopters were used, the FreeFly Alta 6 and a Mikrokopter-based LemHex-44. Both quadcopters used stock-built barometers and cameras while the hexacopters contained a 2-axis gimbal fitted with a Lightware SF11/C laser altimeter and a Sony Alpha A5100 camera with an

APS-C sensor (23.5 mm by 15.6 mm), 6000 x 4000 pixel resolution, and either a Sony SEL 50 mm or SEL 35 mm focal length low distortion lens.

ImageJ 1.5i (Schindelin et al., 2012) was used to measure the total length, maximum body diameter, fluke chord length, and fluke area (Fig. 2). Measurement errors for each aircraft were estimated by measuring a known sized object floating at the surface from various altitudes, and each aircraft had an average altitude error < 5%. Measurements in pixels were multiplied by the ground sampling distance (GSD) to convert to meters following Fearnbach et al. (2012):

$$L_{body} = n_{pix} \times GSD \tag{1}$$

$$GSD = \frac{a}{l_{foc}} \times \frac{S_w}{P_w} \tag{2}$$

where L_{body} is the body length (m), n_{pix} the number of pixels, a the altitude (m), l_{foc} the focal length (mm), S_w the sensor width (mm), and P_w the image resolution width (px). (All equation symbols used in this article are also listed in Table S1). The width of the sensor and image resolution was used since images of the whales were captured full frame widthwise (Gough et al., 2019). In ImageJ (NIH), the combined planar surface area of the flukes (F_a; m^2) was calculated by carefully drawing a polygonal outline of the flukes. Chord length of the flukes (C; m) was measured as the linear distance from the notch between the flukes to the anterior insertion of the flukes on the tail. Body mass (M_{body}; kg) was estimated from total body length using regressions derived for each of our six study species using a broad range of data compiled from both whaling operations and studies of stranded animals (Kahane-Rapport & Goldbogen, 2018). The wetted surface area of the body (S_a; m^2) was estimated from total body length using equations derived from various sources and summarized in Table S2.

Routine and Lunge-Associated Tailbeat Detection

We used a customized MATLAB script to detect tailbeat cycles based upon methods defined by Gough et al. (2019). In particular, a series of thresholds were used to define periods in the filtered (low-pass; 0.44 Hz) gyroscope signal (along the transverse axis) corresponding to individual tailbeats. These thresholds checked for symmetry between the upstroke and downstroke by defining the magnitude, duration, and overall shape of each portion of the tailbeat cycle. The resulting set of tailbeat cycles was spot-checked and compared against tag video to ensure that the parameters were set correctly. Individual whales must have had a dataset of >200 tailbeats in order to be included for further analysis.

Foraging lunges were detected manually using a series of defined kinematic parameters that have been validated using tag video (Cade et al., 2016). These events typically involve an increase in speed during prey approach, followed by a rapid deceleration as an animal opens its mouth to engulf prey (Potvin et al., 2009; Goldbogen et al., 2011; Cade et al., 2016; Potvin et al., 2021). We standardized the period from 10 to 0 seconds prior to the lunge deceleration (which typically coincides with the period of mouth opening) as the lunge-associated period. This length of time corresponds to the approximate length of the acceleration period for a minke whale and the duration of two cruising tailbeats for a blue whale. By choosing this period immediately prior to the lunge for each species in our dataset, we can capture full tailbeats that display high swimming speeds, but a fully closed mouth and hydrodynamic profiles similar to that of routine swimming. We observed that whales do not commonly fluke with their mouth open or during subsequent filtration, but we explicitly excluded any tailbeats during these periods to avoid high drag from the distended throat pouch. Any tailbeat that occurred within the lunge-associated time

period was classified as lunge-associated. All other tailbeats were classified as routine

swimming. The lunge-associated tailbeats included a greater change in swimming velocity, but

our tailbeat detection thresholds ensured general consistency in the overall kinematic profile of

the tailbeats and resulted in two sets of tailbeats at different levels of swimming effort.

Thrust Power, Efficiency, and Drag Coefficient Modeling

For each routine and lunge-associated tailbeat, we measured the mean swimming velocity

(U_{avg}; m s^{-1}) by averaging across the entire time course of the cycle. Since the measurement of

speed by the tag required turbulent flow, speed measurements were limited to >1 m s^{-1} (Cade et

al., 2018). We also measured oscillatory frequency (f; Hz) as the inverse of the duration of the

tailbeat cycle (T_{beat}; s). For routine tailbeats, we calculated (mechanical) thrust power ($\bar{P}_T$; W),

coefficient of drag (C_D), and Froude efficiency (η) based on a model of lunate tail propulsion

using unsteady wing lifting surface theory (Chopra & Kambe, 1977; Yates, 1983; Fish, 1998).

This model begins with the estimation of two input parameters, namely the reduced frequency

(σ) defined as:

$$\sigma = \frac{\omega C}{U_{avg}} \tag{3}$$

where ω is the angular frequency of fluking (with $\omega = 2\pi f$); and the feathering parameter (θ)

defined as:

$$\theta = \frac{\alpha U_{avg}}{\omega h} \tag{4}$$

which is expressed as the ratio of the maximum angle (α; degrees) between the fluke and the direction of motion and the maximum angle ($\omega h/U$) achieved by the trajectory of the pitching axis of the flukes (Yates, 1983) when reaching the heave amplitude (h; m). We were unable to measure precise values for α or h from the tag data and instead relied on validated estimates of 30° for α and one-fifth of body length for h (Bainbridge, 1958; Fish, 1998).

The model devised by Chopra & Kambe (1977) yielded a series of parametric curves expressing the coefficient of thrust (C_T) and Froude efficiency in terms of σ and θ (Yates, 1983). We digitized these curves and estimated both values for each tailbeat cycle, and then estimated the mean thrust force ($\bar{T}$; N) (over a tailbeat cycle) and corresponding mean thrust power ($\bar{P}_T$) as follows (Fish, 1993):

$$\bar{T} = \frac{1}{2} \rho C_T U_{avg}^2 F_a \left(\frac{h}{C} \right)^2 = \frac{\bar{P}_T}{U_{avg}} \tag{5}$$

where ρ is the density of seawater (Table S1). Previous versions of this model assumed steady-state swimming during which the energy gained through propulsion (thrust) matches what is lost through drag, an equality from which the drag coefficient could be obtained (Fish, 1993; 1998). Given the high speed variability inherent in natural tail-heaving swimming, the relationship between mean thrust and mean drag had to be re-written to account for the body's forward acceleration or deceleration during a tailbeat. We started with the equation of motion of the body averaged over the duration of a beat, namely,

$$M_{body} \bar{a} = \bar{T} - \bar{D} \tag{6}$$

where the mean acceleration is given by $\bar{a} = \left(U_f - U_i\right)/T_{beat} \equiv \Delta U/T_{beat}$, with U_f as the final

speed at the end of the tailbeat, U_i the initial speed at its beginning, and T_{beat} as its duration.

Given the high-degree of body streamlining, the mean drag force ($\bar{D}$; N) is expressed as follows

(Goldbogen et al 2019; Potvin et al, 2020; Segre et al, 2020; Potvin et al., 2021):

$$\bar{D} = \frac{1}{2}\rho S_a C_D U_{avg}^2 + k_{added} M_{body} \frac{\Delta U}{T_{beat}} \tag{7}$$

a result involving the corresponding "mean drag coefficient" across the duration of the tailbeat

(C_D). The parameter k_{added} is an acceleration reaction coefficient set at 0.03 for blue whales and

minke whales and 0.05 for humpback whales (Potvin et al, 2020; 2021). Merging equations 5-7

and solving for the drag coefficient result in:

$$C_D = \left(\frac{\bar{P}_T - (k_{added} + 1)M_{body}\left(\frac{\Delta U}{T_{beat}}\right)U_{avg}}{\frac{1}{2}\rho S_a U_{avg}^3} \right) \tag{8a}$$

In this formulation, the tag-measured beat duration (T_{beat}) and change in speed (ΔU) quantifies,

via the second term in the equation, the effects on the drag coefficient of unsteadiness in a

whale's forward speed. Setting it to zero recovers the familiar steady-state case.

For each whale, we found the mean drag coefficient across all routine tailbeats ($C_D^{routine}$) and used that value to estimate the mean thrust power ($\bar{P}_T^{lunge}$; W) for each lunge-associated tailbeat. This calculation involved reordering equation 8a to solve for the mean thrust power:

$$\bar{P}_T^{lunge} = \frac{1}{2}\rho S_a C_D^{routine} U_{avg}^3 + (k_{added} + 1) M_{body} \frac{\Delta U}{T_{beat}} U_{avg} \tag{8b}$$

As a final note, it should be mentioned that estimating the thrust via equation 5 and the graphs found in Yates (1983) represent the closest approximation possible at the present time.

Comparison to a Simple Rigid-Body Model

Cetacean swimming involves body and tail heaving motions that are altogether absent with the motions of rigid bodies (e.g., submarines) and significantly increase drag (Fish, 1993; Fish, 1998; Fish & Rohr, 1999). We compared our drag coefficient data with that of airship models tested in wind tunnels (and at constant wind speed), as correlated by the following correlation (Hoerner, 1965; Webb, 1975; Blevins, 1984; Kooyman, 1989):

$$C_D^{mod} = \left[\frac{0.072}{(Re)^{\frac{1}{5}}}\right] \times \left[1 + 1.5 \left(\frac{W_{max}}{L_{body}}\right)^{\frac{3}{2}} \times 7.0 \left(\frac{W_{max}}{L_{body}}\right)^3\right] \tag{9}$$

Where C_D^{mod} is the modeled drag coefficient and W_{max} is the maximum body diameter (m). This equation is expressed in terms of the Reynold's number (Re):

$$Re = \frac{L_{body} U_{avg}}{\nu} \qquad (10)$$

in which ν is the kinematic viscosity. In this case the drag force ($F_{drag}^{parasite}$) sustained by the

airship (or non-tail-heaving whale) is given by:

$$F_{drag}^{parasite} = \frac{1}{2} \rho S_a C_D^{mod} U^2 \qquad (11)$$

Table S1 contains a list of all symbols used throughout this manuscript.

Statistical Analyses

For our analyses of mean swimming speed and oscillatory frequency against body length,

continuous variables (body length, oscillatory frequency, and mean swimming speed) were $\log^{10}$

-transformed before inclusion as predictors or response variables to normalize our data and

conform to the model of scaling as a power function. For these analyses, we created linear

mixed-effects models with body length as the predictor, oscillatory frequency and mean

swimming speed as response variables, and species as a random effect. For subsequent analyses,

we created linear mixed-effects models with body length, mean swimming speed, and Reynold's

number as predictors, thrust power, drag coefficient, and Froude efficiency as response variables,

and species as a random effect. These models were created using using R v. 3.6 and RStudio

(Version 1.2.1335, packages: ggpubr, and tidyverse) (R Core Team, 2014; Wickham et al., 2019;

Kassambara, 2020). We fitted linear regressions to assess relationships using package lme4 in R.

For our analysis of swimming speed vs Froude efficiency, we used a generalized additive model

(GAM) in R (y ~ s[x, bs = "cs"]).

Results

Kinematic and Morphometric Summary

We investigated interspecific relationships between 65 animals and found that mean ($\pm$ se) values for oscillatory frequency (Hz) and swimming speed (m s^{-1}) both increased when transitioning from routine to lunge-associated swimming. The mean increase in (time-averaged) swimming speed between the two modes was 0.762 ± 0.154 m s^{-1} and the mean increase in oscillatory frequency was 0.102 ± 0.017 Hz (Table 1).

We found that the mean oscillatory frequency for the three species with the most data (humpback, blue, Antarctic minke) decreased with increasing body length, with the Antarctic minke whale having the highest values (routine: 0.38 ± 0.011 Hz; lunge-associated: 0.49 ± 0.008 Hz), followed by the humpback whale (routine: 0.24 ± 0.007 Hz; lunge-associated: 0.34 ± 0.011 Hz) and the blue whale (routine: 0.18 ± 0.004 Hz; lunge-associated: 0.24 ± 0.004 Hz). We found that Bryde's and fin whales had similar routine oscillatory frequencies as the humpback whale while having longer average body lengths (Bryde's: 12.04 ± 2.07 m; fin: 18.90 ± 0.43 m) than the humpback whales in our study (11.06 ± 0.35 m). Both of the oscillatory frequency values for the lone tagged sei whale (routine: 0.22 Hz; lunge-associated: 0.30 Hz) fell approximately halfway between the values for the humpback and blue whales, which aligns with the sei whale's body length (16.62 m) being approximately halfway between the mean humpback and blue whale (22.41 ± 0.33 m) body lengths. We found significant negative relationships between oscillatory frequency and body size during both routine and lunge-associated swimming (routine: $\hat{y}$ = -0.565x + 0.003; R^2 = 0.75; p < 0.001; lunge-associated: $\hat{y}$ = -0.560x + 0.312; R^2 = 0.77; p < 0.001; Fig. 3A).

The mean values for both routine and lunge-associated swimming speeds were similar for the humpback (routine: 2.09 ± 0.066 m s^{-1}; lunge-associated: 2.81 ± 0.100 m s^{-1}), blue (routine: 2.20 ± 0.054 m s^{-1}; lunge-associated: 3.06 ± 0.057 m s^{-1}), and Antarctic minke whales (routine: 2.35 ± 0.052 m s^{-1}; lunge-associated: 2.96 ± 0.118 m s^{-1}). Despite low sample sizes, the average routine and lunge-associated swimming speeds for the Bryde's whale (routine: 1.71 ± 0.47 m s^{-1}; lunge-associated: 3.11 ± 0.629 m s^{-1}) and the routine swimming speed for the sei whale (2.21 m s^{-1}) aligned with the humpback, blue, and Antarctic minke whales, while the lunge-associated swimming speed for the sei whale (2.46 m s^{-1}) was lower than other values and both swimming speeds were higher for the fin whale (routine: 2.88 ± 0.020 m s^{-1}; lunge-associated: 3.61 ± 0.900 m s^{-1}). The average routine swimming speed across all species was found to be 2.18 ± 0.001 m s^{-1}. The median routine swimming speed across all species was found to be 2.06 m s^{-1}. Our statistical analysis found no effect of body size on swim speed for both routine and lunge-associated swimming (routine: $\hat{y} = -0.001x + 0.774$; $R^2 = 6.27 \times 10^{-6}$; $p = 0.984$; lunge-associated: $\hat{y} = 0.080x + 0.862$; $R^2 = 0.04$; $p = 0.091$; Fig. 3B).

The mean percentage change in swimming speed (ΔU) was found to be lower for routine swimming (11.79 ± 1.314 %) than for lunge-associated swimming (24.02 ± 2.162 %). Among the six species, the blue whale displayed the highest ΔU as a value and as a percentage for both routine (0.15 ± 0.027 m s^{-1}; 16.04 ± 0.875 %) and lunge-associated swimming (0.80 ± 0.038 m s^{-1}; 32.09 ± 1.369 %). The other five species did not display a consistent order for ΔU as a value or as a percentage or between routine and lunge-associated swimming. For routine swimming, the fin whale had the second highest ΔU as a percentage (15.06 ± 1.256 %) and the only negative mean value (-0.07 ± 0.030 m s^{-1}), the humpback, Antarctic minke, and sei whales had similar ΔU as a percentage (humpback: 11.60 ± 0.900 %; Antarctic minke: 10.89 ± 0.473 %; sei: 9.59 %)

with the humpback and sei whales having slightly higher values (humpback: 0.08 ± 0.012 m s^{-1}; sei: 0.09 m s^{-1}) than the Antarctic minke whale (0.06 ± 0.009 m s^{-1}), and the Bryde's whale had the lowest ΔU as a value and as a percentage (0.05 ± 0.028 m s^{-1}; 7.62 ± 0.153 %). For lunge-associated swimming, the Bryde's and humpback whales had the second and third highest ΔU values (Bryde's: 0.53 ± 0.134 m s^{-1}; humpback: 0.46 ± 0.055 m s^{-1}) but a flipped order for the percentages (Bryde's: 25.79 ± 5.881 %; humpback: 26.68 ± 1.899 %), the fin whale had the fourth largest ΔU as both a value and a percentage (0.40 ± 0.412 m s^{-1}; 22.43 ± 0.393 %), and the Antarctic minke and sei whales had very similar ΔU values (Antarctic minke: 0.36 ± 0.068 m s^{-1}; sei: 0.37 m s^{-1}) with the Antarctic minke whale having a higher percentage (19.80 ± 1.272 %) than the sei whale (17.33 %). These ΔU-values in turn yielded values of the unsteady-motion correction to C_D^{avg} (i.e., the second term on the right-hand-side of equation (8a)), estimated at 59.10 ± 23.57 % for the humpback whale, 28.5 ± 5.48 % for the blue whale, 15.14 ± 22.39 % for the Antarctic minke whale, 8.98 % for the sei whale, 5.16 ± 1.99 % for the Bryde's whale, and 2.48 ± 1.46 % for the fin whale.

All species-level means ($\pm$ se) for each of our measured kinematic and morphometric variables are given in Table 1. The equations and statistics pertaining to our models are given in Table 2.

Mass-Specific Mechanical Thrust Power Output

Among the three species with a large amount of data in our dataset (humpback, blue, and Antarctic minke whales) and during routine swimming, the humpback whale had the lowest mean mass-specific thrust power output (0.27 ± 0.023 Watts kg^{-1}), with the Antarctic minke whale having a slightly higher value (0.31 ± 0.023 Watts kg^{-1}) and the blue whale having the highest value (0.42 ± 0.024 Watts kg^{-1}). The Bryde's (0.44 ± 0.167 Watts kg^{-1}), sei (0.48), and fin whale (0.64 ± 0.229 Watts kg^{-1}) each had higher values. During lunge-associated swimming, the sei whale had the lowest value (0.87), with the Antarctic minke (1.23 ± 0.150 Watts kg^{-1}) and humpback whales (1.30 ± 0.138 Watts kg^{-1}) having similar values and the blue (1.85 ± 0.111 Watts kg^{-1}), fin (2.04 ± 1.293 Watts kg^{-1}), and Bryde's (3.03 ± 0.527 Watts kg^{-1}) whales all having higher values.

Mean mass-specific thrust power output increased with the transition from routine to lunge-associated swimming modes (Fig. 4A-B), and to values in agreement with an alternative approach based on the work-energy theorem (Potvin et al, 2021). There was a positive effect of swimming speed on mass-specific thrust power output during both routine and lunge-associated swimming (routine: $\hat{y} = 0.381x - 1.215$; $R^2 = 0.38$; $p < 0.001$; lunge-associated: $\hat{y} = 0.320x - 0.804$; $R^2 = 0.57$; $p < 0.001$; Fig 4A). We also found that mean mass-specific thrust power output increases with body length for both routine ($\hat{y} = 0.015x - 0.705$; $R^2 = 0.24$; $p < 0.001$) and lunge-associated swimming ($\hat{y} = 0.011x - 0.019$; $R^2 = 0.12$; $p = 0.005$; Fig. 4B). The species-level means ($\pm$ se) for each of our measured hydrodynamic parameters are given in Table 3.

Drag Coefficient

Among humpback, blue, and Antarctic minke whales, the Antarctic minke whale had the lowest mean drag coefficient (0.008 ± 0.001), with the humpback whale slightly higher (0.0015 ± 0.001) and the blue whale having the highest value (0.030 ± 0.003). We found that the drag coefficient for routine swimming decreased with increasing swim speed (routine: $\hat{y} = -0.011x + 0.043$; $R^2 = 0.09$; $p = 0.015$; Fig 5A). Conversely, the drag coefficient increased for routine swimming with increasing total body length (routine: $\hat{y} = 0.002x - 0.002$; $R^2 = 0.50$; $p < 0.001$; Fig 5B).

We found that the drag coefficient increased significantly with Reynolds number (routine: $\hat{y} = 5.23*10^{-10}x - 3.36*10^{-3}$; $R^2 = 0.31$; $p < 0.001$; Fig 5C). In comparison to the R-100 rigid-hulled airship model, all species displayed higher drag coefficients by an approximate factor of 3 for the Antarctic minke whale and as high as 14 for the Bryde's whale (Fig 5C) which are consistent with the discrepancies found among odontocetes (Fish 1993, 1998; Fish et al, 2014) .

Froude Efficiency

Of the three species with a large quantity of data in our dataset (humpback, blue, and Antarctic minke whales), the Antarctic minke whale had the highest mean Froude efficiency during routine swimming (0.920 ± 0.004), with the humpback whale having a lower mean value (0.909 ± 0.003) and the blue whale having the lowest mean value (0.863 ± 0.004). The mean values for the Bryde's (0.868 ± 0.022), sei (0.878), and fin whales (0.889 ± 0.018) were all near the low end of the range.

We found that mean Froude efficiency increases with increasing swimming speed up to an approximate plateau at ~3 m s^{-1} (Fig. 6A). On the other hand, we found that mean Froude efficiency decreased with increasing body length (routine: $\hat{y}$ = -0.004x – 0.950; R^2 = 0.68; $p <$ 0.001; Fig. 6B). As compared to prior studies, our results demonstrate that, regardless of body size, rorqual whales demonstrate high efficiency (>75%) comparable to other oscillatory swimmers (Fig. 7). Sub-carangiform, undulatory swimmers such as the rainbow trout (*Oncorhynchus mykiss*) are slightly lower (~60-80%) and drag-based swimmers, such as the muskrat and human, have much lower Froude efficiencies (~20-35%) (Fig. 7). Table S3 gives additional information about each literature-based mean Froude efficiency value.

Discussion

Many previous studies that have quantified the kinematics and hydrodynamics of cetacean swimming have used captive animals that can be measured reliably from a stable reference position (Fish, 1993; Fish, 1998; Rohr & Fish, 2004). By comparison, the present study is a first approximation for many of the same kinematic variables of much larger species in their natural environment. Several parameters, such as the angle of attack of the flukes relative to the body or the amplitude of heave are still generally unknown (except in rare circumstances, see Gough et al., 2019), so we supplemented our empirical data with validated estimates for these unknown variables (Bainbridge, 1958; Fish, 1998). The angle of attack of the fluke has been found to change with speed over a range from 20-40°, so we used 30° as an average value (Fish, 1998). Amplitude of heave has been reliably measured as one-fifth of body length and remains constant across swimming speeds and body size (Bainbridge, 1958; Fish, 1998). Our

combination of empirical measurements and reliable estimates allowed us to quantify

hydrodynamic and kinematic aspects of mysticete swimming using a numerical computation

based on unsteady lifting-surface theory and derived by Chopra & Kambe (1977), which has also

been validated for odontocetes by Fish (1998). The similarity between our methods and those of

previous studies extends our ability to compare swimming performance across vast body size

ranges.

Oscillatory Frequency and Swimming Speed

Our results illustrate that the transition from routine to lunge-associated swimming

predictably results in increased oscillatory frequencies and swimming speeds as the animal

prepares for a lunge (Fig. 3) (Goldbogen et al., 2011; Cade et al., 2016). Gough et al. (2019)

found that the oscillatory frequency decreases with increasing body size to the power of -0.53,

and with a more robust data set we have found similar scaling exponents of -0.565 and -0.560 for

routine and lunge-associated swimming, respectively. For swimming speed, we again found

similar results to Gough et al. (2019) with swimming speed remaining consistent at ~2 m s^{-1}. For

both oscillatory frequency and swimming speed, the scaling exponents for routine and lunge-

associated swim efforts were nearly identical, with a difference of 0.005 for oscillatory

frequency and a difference of 0.081 for swimming speed. This suggests that, regardless of body

size, mysticetes prepare for a feeding lunge through similar kinematic pathways which include a

consistent increase in both oscillatory frequency and swimming speed. These results for

oscillatory frequency and swimming speed align with previous results for fish and odontocetes

that have shown that swimming speed is heavily modulated by oscillatory frequency

(Bainbridge, 1958; Fish, 1998; Gough et al., 2019).

Mean Mass-Specific Thrust

Thrust generation is a fundamental aspect of any swimming mode and the achievable thrust for a swimming animal has a direct impact on its maximum swimming speed and, subsequently, the types and quantities of prey that it can capture (Fish, 1998; Potvin et al., 2009; Cade et al., 2020). Hydrodynamic theory states that thrust should increase with the square of velocity (Webb, 1975; Vogel, 1994). Thrust from an oscillating hydrofoil will further increase the thrust of a system by 3-to-5 times (Lighthill, 1971; Liu et al., 1997; Anderson et al., 2001; Fish et al., 2014). While this theory holds for animals of similar sizes, we found it advantageous to measure the mass-specific thrust to make comparisons between mysticetes and other cetaceans that vary across a wide range of body sizes.

For cetaceans, high mass-specific thrust allows odontocetes to capture fast-moving, individual fish (Maresh et al., 2004) and allows mysticetes to achieve high speeds during feeding lunges to offset the deceleration during prey engulfment as well as the potential escape response of different prey types (Cade et al., 2016; Cade et al., 2020). Fish (1998) measured the mass-specific thrust of odontocete species and found maximum mass-specific thrust values of 22.5 and 23.7 W kg^{-1} for *Pseudorca crassidens* and *Tursiops truncatus*, respectively. The maximum mass-specific thrust value for a mysticete (Bryde's) swimming at 6.3 m s^{-1} (lunge-associated) in our study was found to be 16 W kg^{-1}, but mass-specific thrust values at the species-level averaged between 0.87-3.03 W kg^{-1} for lunge-associated swimming and between 0.27-0.64 W kg^{-1} for routine swimming, which were one to two orders of magnitude lower (Fig 4A; Table 3). These results suggest that mysticetes typically maintain low average mass-specific thrust values in accordance with their relatively steady swimming speeds (~1.5-2.5 m s^{-1}), but that they can attain extremely high mass-specific thrust power output when properly motivated. Swimming speeds

higher than those found in our dataset have also been found for humpbacks (up to ~9 m s^{-1}; Tomilin, 1957; Segre et al., 2020), indicating that they could be producing mass-specific thrust values on par with odontocetes during fast maneuvers such as surface breaches.

Our comparisons of speed-matched mass-specific thrust output between routine swimming and lunges suggest that whales likely alter oscillatory frequency in order to generate greater thrust during feeding (Gough et al., 2019). Mass-specific thrust power at a routine swimming speed (~1.5-2.5 m s^{-1}) results in a low propulsive energy cost (Gough et al., 2019). The relative similarity of the mass-specific thrust increase (~two-fold) from routine to a lunge feeding effort across our range in body size suggests that all of the large whales studied are preparing for a lunge in similar ways. Field data (Cade et al., 2020) and hydrodynamic models (Potvin et al., 2009; 2020) suggest that the whales begin lunges at high speeds (3.5-5 m s^{-1}) in order to overcome heightened drag during engulfment and krill-feeders usually move through the prey patch on momentum (Potvin et al., 2009).

Focusing more heavily on the relationship between mass-specific thrust generation and body size, our results diverge slightly from previous estimates. Fish (1998) determined that mass-specific thrust and body size have no relationship. Hill (1950) considered that for similar animals, the maximum power generated during a steady effort would increase not directly with the weight (W), but rather with W$^{0.73}$. As a result, we expected that mass-specific thrust would decrease proportionately with increasing body size. Instead, we found that mass-specific thrust increases as body length increases (Fig. 4). This relationship could result from the higher oscillatory frequencies with larger body sizes that Gough et al. (2019) and our current study found in contrast to previous expectations of oscillatory frequency (Hill, 1950; Sato et al., 2007). For the relationship between oscillatory frequency and body length, Sato et al. (2007) found a

more extreme allometric scaling exponent (approximately -1.0), whereas Gough et al. (2019) and our current study found an exponent of approximately -0.5, suggesting a less extreme decrease in oscillatory frequency with increasing body length.

Drag Coefficient vs. Reynolds Number

In comparison to our tagged animals, Hoerner's R-100 airship model used for computational analysis did not include control surfaces (flippers or flukes). Instead, the approximated environment around the airship was determined using wind tunnel test data (Hoerner, 1965; Blevins, 1984). These modeled values suggest that for an Antarctic minke whale (~5m), the drag coefficients for fluking should be roughly three times higher than non-fluking and gliding. But the difference between these coefficients should increase for larger animals, culminating in a ten-fold difference for a blue whale (~22m) (Fig. 5B). Other studies predicted similar increases in the drag coefficient, with Lighthill (1971) first noticing a discrepancy between the expected drag coefficient based on Hoerner's model and the observed values for swimming fish, but his conclusions did not account for changing Reynolds numbers and were based upon animals swimming at Reynolds numbers of $\sim 10^5$ whereas large cetaceans are routinely swimming at values of $\sim 10^7$. Fish (1993) included a variety of species and groups and found higher drag coefficient values for swimming animals as compared to model estimates, but they did not find an increase with increasing Reynolds number like we have for larger cetaceans (Fig. 5C). Fish (1998) analyzed how the drag coefficient might vary with Reynolds number among four species of odontocetes and found that the drag coefficient should decrease with increasing Reynolds number.

For mysticetes, we found a negative relationship between the drag coefficient and the swimming speed as well as a positive relationship between the drag coefficient and body length (Fig. 5A-B). Reynolds number is affected by both the swimming speed and the body length of an animal, so we believe that the impact of body size between individuals is more extreme than the impact of swimming speed within individuals, resulting in a net positive impact of Reynolds number on drag coefficient (Fig. 5C). The effects of swimming speed on drag coefficient have been determined previously by Fish (1998) for a group of odontocetes, but ours is the first study that includes a large enough body size range to be able to parse out the effect of body size on both Reynolds number and drag coefficient.

Froude Efficiency vs. Swimming Velocity

Optimal locomotor speeds have been demonstrated for runners, flyers, and swimmers (e.g., Tucker, 1968; Webb, 1975; Hoyt & Taylor, 1981; Watanabe et al., 2011). The cost of transport (COT) has been used as the metabolic proxy that is inversely related to the Froude efficiency (Williams et al., 1993; Fish, 2000) and Yazdi et al. (1999) found that the minimum COT for the bottlenose dolphin (*Tursiops truncatus*) occurred at swimming speeds of 2.1 and 2.5 m s^{-1}, respectively. These speeds coincided with the routine swimming speeds in wild populations. Similarly, gray whales (*Eschrichtius robustus*) and Antarctic minke whales cruise at the speed of the lowest COT (Sumich, 1983; Blix & Folkow, 1995). The minimum COT for the gray whale corresponded to the swimming velocity (2.0-2.5 m s^{-1}) of migrations (Wyrick, 1954; Williamson, 1972; Sumich, 1983). Antarctic minke whales, however, were determined to have a minimum COT at the maximum cruising velocity of 3.25 m s^{-1} (Blix & Folkow, 1995), which was 37% higher than the average routine swimming speed (2.35 m s^{-1}) in the present study. This

average velocity was within the range of swimming velocities (1.5-2.6 m s^{-1}) for migrating Antarctic minke whales (Williamson, 1972), a range that accounted for 56.5% of the routine swimming speed measurements for Antarctic minke whales in our dataset. The average routine swimming velocities for blue (2.20 m s^{-1}) and humpback whales (2.09 m s^{-1}) also fell within ranges of migratory velocities of 1.5-3.1 m s^{-1} (Williamson, 1972) and 1.1-4.0 m s^{-1} (Chittleborough, 1953; Williamson, 1972), respectively. These ranges accounted for 67.1% of the routine swimming speed measurements for the blue whales and 99.0% of the same measurements for the humpback whales in our dataset. The average (2.18 m s^{-1}) and median (2.06 m s^{-1}) routine swimming speed that we found among all species fell near the center of these migratory speed ranges and aligned closely with the optimal swimming speed (U_{opt}; 1.97 m s^{-1}) predicted by Gough et al. (2019) (Fig 6A).

Only 1% of our speed measures fell above 4.5 m s^{-1}, meaning our ability to predict Froude efficiency at these high speeds is limited. The significantly unsteady nature of lunge-associated swimming also meant that we could not include that swimming style in our analysis of Froude efficiency. Our results for routine swimming below 4.5 m s^{-1} show that Froude efficiency increases rapidly below ~2 m s^{-1} and plateaus, which broadly agrees with the results from Fish (1998) for ontocetes. The position of the plateau relative to the average routine swimming speed and the optimal swimming speed from Gough et al. (2019) suggests that these species are simultaneously minimizing their swimming speed and maintaining high Froude efficiency along the plateau (Fig 6A).

Froude Efficiency vs. Total Body Length (m)

In this study, Froude efficiency relates to the amount of mechanical work the animal does to propel itself forward. Previous research has shown that Froude efficiency would remain constant or slightly increase with increasing body size (Fish, 1998). However, we found that Froude efficiency decreases with increasing body size among rorquals (See Fig. 7B). The mechanistic explanation of this finding is that larger individuals have a slightly increased thrust generation but a greatly increased drag coefficient (Figs. 4 and 5), thus resulting in a lower Froude efficiency, because more energy may be required to overcome drag and achieve equivalent locomotor performance.

Our analyses suggest that size is an important determinant of swimming efficiency in rorquals. Balaenopteridae exhibit a size range than spans an order of magnitude in body mass, from Antarctic minke whales to blue whales (Lockyer, 1976). The scale of these ocean giants necessitates the use of oscillatory lift-based swimming as an effective propulsive mechanism for high-speed swimming at high Reynolds numbers (Webb & De Buffrénil, 1990; Fish, 2020). Interestingly, in parallel with the trend of maximum speed in which intermediately-sized animals (~250 kg; the approximate size of a common bottlenose dolphin) exhibited the highest performance with lower maximum speeds for small and large animals, it was found for whales that Froude efficiency, another locomotor performance variable, decreased above and below a different and larger optimal size, roughly between a killer whale and a minke whale (Hirt et al., 2017) (Fig. 7; Table S3).

Conclusions

The thrust power and drag coefficient produced by rorquals during routine swimming increased with body size. However, the Froude efficiency was found to decrease with increasing body size. These conclusions ran counter to our expectations of the swimming performance of cruising rorquals. During foraging, these animals swim over a wider speed range and produced greater maximum thrust than exhibited at routine speeds. This difference is predictable due to a higher oscillatory frequency during foraging bouts in which the whale beats its tail faster to accelerate to the high speeds necessary to overcome the increased drag as the mouth opens during engulfment and prey capture. Our results quantify the fine-scale hydrodynamics that underlie these energetic differences between routine swimming and energetically expensive foraging. In addition, we show that large whales – across a range of body sizes – can modulate their swimming kinematics to optimize energy use, but might experience a reduced energy economy as Froude efficiency decreases with increasing body size.

Acknowledgments

19116, 15271, 20430), Canada DFO SARA/MML 2010-01/SARA-106B, National Marine Sanctuaries (MULTI-2017-007), Research permit R23.2018 issued by the Falkland Islands Government, ACA 2015-014, and institutional IACUC committees.

Data Availability

The datasets supporting this article are available from the corresponding author on request and at the following Data Dryad link (doi no.).

Competing Interests

We have no competing interests to report.

Funding

References

1. Anderson, E. J., McGillis, W. R. and Grosenbaugh, M. A. (2001). The boundary layer of swimming fish. *J. Exp. Biol*. **204**: 81-102.

2. Bainbridge, R. (1958). The speed of swimming of fish as related to size and to the frequency and amplitude of the tail beat. *J. Exp. Biol.* **35**: 109-133.

3. Blake, R. W. (1979). The mechanics of labriform locomotion I. labriform locomotion in the angelfish (*Pterophyllum eimekei*): an analysis of the power stroke. *J. Exp. Biol.* **82**: 255–271.

4. Blake, R. W. (1980). The mechanics of labriform locomotion II. an analysis of the recovery stroke and the overall fin-beat cycle propulsive efficiency in the angelfish. *J. Exp. Biol.* **85**: 337–342.

5. Blevins, R. D. (1984). *Applied fluid dynamics handbook*. New York, N.Y: Van Nostrand Reinhold Co.

6. Blickhan, R. and Cheng, J-Y (1994). Energy storage by elastic mechanisms in the tail of large swimmers – a re-evaluation. *J. Theor. Biol.* **168**: 315-321.

7. Blix, A. S. and Folkow, L. P. (1995). Daily energy expenditure in free living minke whales. *Acta Physiol. Scand.* **153**: 61-66.

8. Bose, N. and Lien, J. (1989). Propulsion of a fin whale (*Balaenoptera physalus*): Why the fin whale is a fast swimmer. *P. Roy. Soc. B-Biol. Sci.* **237**: 175–200.

9. Cade, D. E., Friedlaender, A. S., Calambokidis, J., Goldbogen, J. A. (2016). Kinematic diversity in rorqual whale feeding mechanisms. *Curr. Biol.* **26**: 2617-2624.

10. Cade, D.E., Barr, K. R., Calambokidis, J., Friedlaender, A. S. and Goldbogen, J. A. (2018). Determining forward speed from accelerometer jiggle in aquatic environments. *J. Exp. Biol.* **221**, jeb170449.

11. Cade, D. E., Carey, N., Domenici, P., Potvin, J., and Goldbogen, J. A. (2020) Predator-informed looming stimulus experiments reveal how large filter feeding whales capture highly maneuverable forage fish. *Proc. Nat. Acad. Sci.* **117**: 472-478.

12. Chittleborough, R. G. (1953). Aerial observations on the humpback whales, *Megaptera nodosa* (Bonnaterre), with notes on other species. *Aust. J. Mar.Freshwater Res.* **4**: 219-226.

13. Chopra, M. G. and Kambe, T. (1977). Hydromechanics of lunate-tail swimming propulsion. Part 2. *J. Fluid Mech*. **79**: 49-69.

14. Christiansen, F., Sironi, M., Moore, M.J., Di Martino, M., Ricciardi, M., Warick, H.A., Irschick, D.J., Gutierrez, R. and Uhart, M.M., 2019. Estimating body mass of free- living whales using aerial photogrammetry and 3D volumetrics. *Methods Ecol. Evol.* **10**: 2034-2044.

15. Curren, K. C., Bose, N., and Lien, J. (1994). Swimming kinematics of a harbor porpoise (*Phocoena phocoena*) and an Atlantic white- sided dolphin (*Lagenorhynchus acutus*). *Mar. Mamm. Sci.* **10**: 485–492.

16. Donley, J. M., Sepulveda, C. A., Konstantinidis, P., Gemballa, S. and Shadwick, R. E. (2004). Convergent evolution in mechanical design of lamnid sharks and tunas. *Nature.* **429**, 61-65.

17. Fearnbach, H., Durban, J., Parsons, K., and Claridge, D. (2012). Photographic mark–recapture analysis of local dynamics within an open population of dolphins. *Ecol. Appl.* **22**(5): 1689-1700.

18. Fish, F. E. (1984). Mechanics, power output and efficiency of the swimming muskrat (*Ondatra zibethicus*). *J. Exp. Biol.* **110**: 183-201.

19. Fish, F. E. (1993). Power output and propulsive efficiency of swimming bottlenose dolphins (*Tursiops truncatus*). *J. Exp. Biol.* **185**: 179-193.

20. Fish, F. E. (1998). Comparative kinematics and hydrodynamics of odontocete cetaceans: morphological and ecological correlates with swimming performance. *J. Exp. Biol.* **201**: 2867-2877.

21. Fish, F. E. (2000). Biomechanics and energetics in aquatic and semiaquatic mammals: Platypus to whale. *Physiol. Biochem. Zool*. **73**: 683-698.

22. Fish, F. E. (2020). Aquatic animals operating at high Reynolds numbers: Biomimetic opportunities for AUV applications. P.p. In press. In: Bioinspired Design (W. Soboyejp, ed.), Cambridge University Press, Cambridge.

23. Fish, F. E. and Battle, J. M. (1995). Hydrodynamic design of the humpback whale flipper. *J. Morph.* **225**, 51-60.

24. Fish F. E., Howle, E. L., Murray, M. M. (2008). Hydrodynamic flow control in marine mammals, *Integr. Comp. Biol.* **48**: 788–800.

25. Fish, F. E., Innes, S. and Ronald, K. (1988). Kinematics and estimated thrust production of swimming harp and ringed seals. *J. Exp. Biol.* **137**: 157–173.

26. Fish, F. E., Legac, P., Williams, T. M. and Wei, T. (2014). Measurement of hydrodynamic force generation by swimming dolphins using bubble DPIV. *J. Exp. Biol.* **217**: 252-260.

27. Fish, F.E. and Rohr, J.J. (1999). *Review of dolphin hydrodynamics and swimming performance. SPAWARS System Center Technical Report* 1801, San Diego, CA.

28. Gleiss, A. C., Jorgensen, S. J., Liebsch, N., Sala, J. E., Norman, B., Hays, G.C., Quintana, F., Grundy, E., Campagna, C., Trites, A.W., Block, B.A. and Wilson, R.P. (2011). Convergent evolution in locomotory patterns of flying and swimming animals. *Nature Comms.* **2**: 1-7.

29. Goldbogen, J. A., Cade, D. E., Boersma, A. T., Calambokidis, J., Kahane-Rapport, S. R., Segre, P. S., Stimpert, A. K. and Friedlaender, A. S. (2017a). Using digital tags with integrated video and inertial sensors to study moving morphology and associated function in large aquatic vertebrates. *Anat. Rec.* **300**: 1935-1941.

30. Goldbogen, J.A., Cade, D.E., Calambokidis, J., Friedlaender, A.S., Potvin, J., Segre, P.S. & Werth, A.J. (2017b) How Baleen Whales Feed: The Biomechanics of Engulfment and Filtration. *Annual review of marine science,* **9,** 1-20.

31. Goldbogen, J. A., Cade, D. E., Wisniewska, D. M., Potvin, J., Segre, P. S., Savoca, M. S., Hazen, E. L., Czapanskiy, M. F., Kahane-Rapport, S. R., DeRuiter, S. L., Gero, S., Tønnesen, P., Gough, W. T., Hanson, M. B., Holt, M. M., Jensen, F. H., Simon, M., Stimpert, A. K., Arranz, P., Johnston, D. W., Nowacek, D. P., Parks, S. E., Visser, F., Friedlaender, A. S., Tyack, P. L., Madsen, P. T. and Pyenson, N. D. (2019). Why whales are big but not bigger: Physiological drivers and ecological limits in the age of ocean giants. *Science* **366**: 1367-1372.

32. Goldbogen, J. A., Calambokidis, J., Oleson, E., Potvin, J., Pyenson, N. D., Schorr, G., & Shadwick, R. E. (2011). Mechanics, hydrodynamics and energetics of blue whale lunge feeding: efficiency dependence on krill density. *J. Exp. Biol.* **214**: 121-146.

33. Gough, W. T., Segre, P. S., Bierlich, K. C., Cade, D. E., Potvin, J., Fish, F. E., Dale, J., di Clemente, J., Friedlaender A. S., Johnston D. W., Kahane-Rapport, S. R., Kennedy, J., Long J. H., Oudejans, M., Penry, G., Savoca, M. S., Simon, M., Videsen, S. K. A., Visser, F., Wiley, D. N. and Goldbogen, J. A. (2019). Scaling of swimming performance in the largest animals. *J. Exp. Biol.* **222**: jeb204172.

34. Hill, A. V. (1950). The dimensions of animals and their muscular dynamics. *Sci. Prog*. **38**: 209-230.

35. Hirt, M. R., Jetz, W., Rall, B. C. and Brose, U. (2017). A general scaling law reveals why largest animals are not the fastest. *Nat. Ecol. Evol*. **1**: 1116-1122.

36. Hoerner, S. F. (1965). Fluid dynamic drag. Published by author, Midland Park, NJ.

37. Hoyt, D. F. and Taylor, C. R. (1981). Gait and the energetics of locomotion in horses. *Nature* **292**: 239-240.

38. Johnson, M.P. & Tyack, P.L. (2003) A digital acoustic recording tag for measuring the response of wild marine mammals to sound. *IEEE Journal of Oceanic Engineering,* **28,** 3-12.

39. Kahane- Rapport, S. R. and Goldbogen, J. A. (2018). Allometric scaling of morphology and engulfment capacity in rorqual whales. *J. Morph*. **279**: 1256-1268.

40. Kahane-Rapport, S. R., Savoca, M. S., Cade, D. E., Segre, P. S., Bierlich, K. C., Calambokidis, J., Dale, J., Fahlbusch, J. A., Friedlaender, A. S., Johnston, D. W., Werth, A. J. and Goldbogen, J. A. (2020). Lunge filter feeding biomechanics constrain rorqual foraging ecology across scale. *J. Exp. Biol.* **279**, jeb.224196.

41. Kassambara, A. (2020). ggpubr: 'ggplot2' Based Publication Ready Plots. Cran.R-Projects. Version 0.4.0.

42. Kelley, N. and Pyenson, N. (2015). Vertebrate evolution. Evolutionary innovation and ecology in marine tetrapods from the Triassic to the Anthropocene. *Science* **348**: 301-308.

43. Kennedy, J. H. (2021) .Hydrodynamics of Rorquals. Ph.D. Dissertation, Saint Louis University.

44. Kermack, A. K. (1948). The propulsive powers of blue and fin whales. *J. Exp. Biol.*1948 25: 237-240.

45. Kojeszewski, T. and Fish, F.E. (2007). Swimming kinematics of the Florida manatee (*Trichechus manatus latirostris*): hydrodynamic analysis of an undulatory mammalian swimmer. *J. Exp. Biol.* **210**: 2411–2418.

46. Kooyman, G. L. (1989). Diverse divers: physiology and behavior. Berlin: Springer-Verlag.

47. Krogh, A. (1934). Conditions of life at great depths in the ocean. Ecol. Mongraphs 4: 430-439.

48. Lighthill, J. (1971). Large-amplitude elongate-body theory of fish locomotion. *Proc. R. Soc. B* **179**: 125-138.

49. Liu, H., Wassersug, R. J. and Kawachi, K. (1997). The three-dimensional hydrodynamics of tadpole locomotion. *J. Exp. Biol*. **200**: 2807-2819.

50. Lockyer, C. (1976). Body weights of some species of large whales. *ICES J. Mar. Sci.* **36**: 259-273.

51. Magnuson, J. J. (1978). Locomotion by Scombrid Fishes: Hydromechanics, Morphology, and Behavior. In *Fish Physiology*. 239–313. Elsevier.

52. Maresh, J. L., Fish, F. E., Nowacek, D. P., Nowacek, S. M. and Wells, R. S. (2004). High performance turning capabilities during foraging by bottlenose dolphins (*Tursiops truncatus*). *Mar. Mamm. Sci*. **20**: 498-509.

53. McCutchen, C. W. (1975). Froude propulsive efficiency of a small fish, measured by wake visualization. *Scale effects in animal locomotion.* 339-363. Academic Press London, New York.

54. Motani, R. (2002). Scaling effects in caudal fin propulsion and the speed of ichthyosaurs. *Nature* **415**: 309-312.

55. Parry, D.A. (1949). The swimming of whales and a discussion of Gray's paradox. *J. Exp. Biol.* **26**: 24-28.

56. Potvin, J., Cade, D.E., Werth, A.J., Shadwick, R.E. and Goldbogen, J.A., 2020. A perfectly inelastic collision: Bulk prey engulfment by baleen whales and dynamical implications for the world's largest cetaceans. *Am. J. Phys.* **88:** 851-863.

57. Potvin, J., Cade, D.E., Werth, A.J., Shadwick, R.E. and Goldbogen, J.A., 2021. Rorqual Lunge-Feeding Energetics Near and Away from the Kinematic Threshold of Optimal Efficiency. *Integr. Org. Biol.* In Press.

58. Potvin, J., Goldbogen, J. A. and Shadwick, R. E. (2009). Passive versus active engulfment: verdict from trajectory simulations of lunge-feeding fin whales Balaenoptera physalus. *J. Roy. Soc. Interf*ace **6**: 1005-1025.

59. R Core Team (2014). R: A language and environment for statistical computing. R Foundation for Statistical Computing, Vienna, Austria. URL http://www.R-project.org/.

60. Rohr, J. and Fish, F. E. (2004). Strouhal numbers and optimization of swimming by odontocete cetaceans. *J. Exp. Biol*. **207**: 1633-1642.

61. Sato, K., Watanuki, Y., Takahashi, A., Miller, P.J.O., Tanaka, H., Kawabe, R., Ponganis, P.J., Handrich, Y., Akamatsu, T., Watanabe, Y., Mitani, Y., Costa, D.P., Bost, C.A., Aoki, K., Amano, M., Trathan, P., Shapiro, A. and Naito, Y. (2007). Stroke frequency, but not swimming speed, is related to body size in free-ranging seabirds, pinnipeds and cetaceans. *Proc. R. Soc. Lond. B*. **274**: 471-477.

62. Schindelin, J., Arganda-Carreras, I., Frise, E., Kaynig, V., Longair, M., Pietzsch, T., Preibisch, S., Rueden, C., Saalfeld, S., Schmid, B. et al. (2012). Fiji: an open-source platform for biological-image analysis. *Nat. Methods* **9**: 676-682.

63. Segre, P. S., Potvin, J., Cade, D. E., Calambokidis, J., Di Clemente, J., Fish, F. E., Friedlaender, A. S., Gough, W. T., Kahane-Rapport, S. R., Oliveira, C., Parks, S. E., Penry, G. S., Simon, M., Stimpert, A. K., Wiley, D. N., Bierlich, K. C., Madsen, P. T. and Goldbogen, J. A. (2020). Energetic and physical limitations on the breaching performance of large whales. *eLife*. **9**: e51760.

64. Slater G. J., Goldbogen J. A. and Pyenson N. D. (2017). Independent evolution of baleen whale gigantism linked to PlioPleistocene ocean dynamics. *Proc. R. Soc. B* **284**: 20170546.

65. Sloop L. J., (1978). Appendix B: Liquid Hydrogen as a Propulsion Fuel, 1945-1959. NASA SP-4404, 324 pages, NASA, Washington, D.C.

66. Sumich, J. L. (1983). Swimming velocities, breathing patterns, and estimated costs of locomotion in migrating gray whales, *Eschrichtius robustus*. *Can. J. Zool*. **61**: 647-652.

67. Taylor, G. K., Nudds, R. L. and Thomas, A. L. R. (2003). Flying and swimming animals cruise at a Strouhal number tuned for high power efficiency. *Nature*. **425**: 707-711.

68. Tomilin, A.G. (1957). *Mammals of the USSR and Adjacent Countries*. Volume IX, Cetacea. Izdatel'stvo Akademi Nauk SSSR, Moskva (Translated from Russian).

69. Triantafyllou, M. S., Triantafyllou, G. S. and Gopalkrishnan, R. (1991). Wake mechanics for thrust generation in oscillating foils. *Phys. Fluids.* **3**: 2835-2837.

70. Tucker, V. A. (1968). Respiratory exchange and evaporative water loss in the flying budgerigar. *J. Exp. Biol*. **48**: 67-87.

71. Vogel, S. (1994). *Life in Moving Fluids*. Princeton, NJ: Princeton University Press.

72. Von Loebbecke, A., Mittal, R., Fish, F. and Mark, R. (2009). Propulsive efficiency of the underwater dolphin kick in humans. *J. Biomech. Eng.* **131**: 054504-1-054504-4.

73. Watanabe, Y.Y., Sato, K., Watanuki, Y., Takahashi, A., Mitani, Y., Amano, M., Aoki, K., Narazaki, T., Iwata, T., Minamikawa, S. and Miyazaki, N. (2011). Scaling of swim speed in breath-hold divers. *J. Anim. Ecol.* **80**: 57-68.

74. Webb, P. W. (1975). Hydrodynamics and energetics of fish propulsion. *Bull. Fish. Res. Board Can.* **190**: 1–159.

75. Webb, P. W. and De Buffrénil, V. (1990). Locomotion in the biology of large aquatic vertebrates. *Trans. Am. Fish. Soc*. **119**: 629-641.

76. Wickham et al., (2019). Welcome to the Tidyverse. *J. Open Source Software* **4**: 1686.

77. Williams, T. M., Friedl, W. A., and Haun, J. (1993). Balancing power and speed in bottlenose dolphins (*Tursiops truncatus*). *Symp. Zool. Soc. Lond*. 66: 383-394.

78. Williamson, G. R. (1972). The true body shape of rorqual whales. *J. Zool., Lond*. **167**: 277-286.

79. Woodward, B. L., Winn, J. P. and Fish, F. E. (2006). Morphological specializations of baleen whales associated with hydrodynamic performance and ecological niche. *J. Morph*. **267**: 1284-1294.

80. Wyrick, R. F. (1954). Observations on the movements of the Pacific gray whale *Eschrichtius robustus* (Cope). *J. Mamm*. **35**: 596-598.

81. Yates, G. T. (1983). Hydrodynamics of body and caudal fin propulsion. In *Fish Biomechanics* (ed. P. W. Webb and D. Weihs), pp. 177–213. New York: Praeger.

82. Yazdi, P., Kilian, A. and Culik, B. (1999). Energy expenditure of swimming bottlenose dolphins (*Tursiops truncatus*). *Mar. Biol*. **134**; 601-607.

Figures
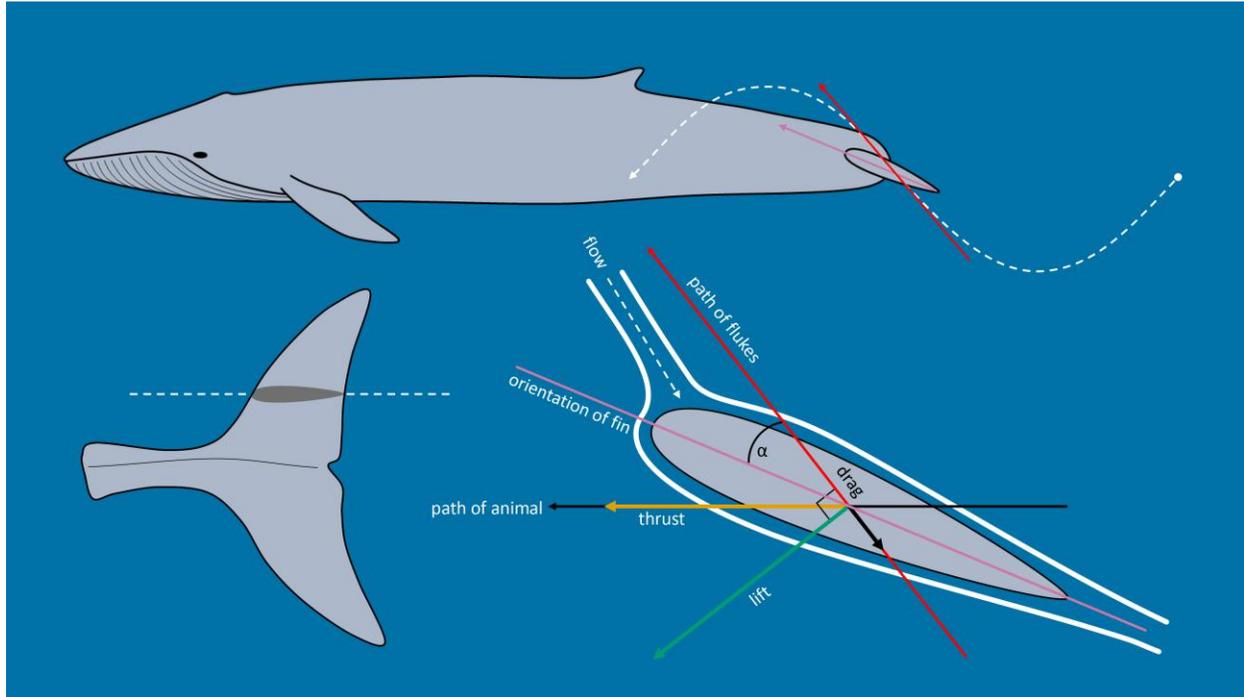
Figure 1. Adaptation from Shadwick (2005) showing the forces acting on the tail of a thunniform swimmer such as a blue whale during active oscillatory fluking of the tail. The heaving motion of the tail creates a pressure imbalance between the top and bottom faces of the fluke that results in the generation of a lift force perpendicular to the path of the flukes and a thrust force in the forward direction of travel of the animal.

Figure 2. Representative UAS drone image of a humpback whale showing the morphometric measurements taken from each animal. The white line corresponds to the total length (in meters) from the tip of the lower jaw to the caudal midpoint of the tail. The chord length of the fluke (in meters) is denoted by the red line running from the cranial insertion of the fluke onto the peduncle to the caudal midpoint of the tail. The light orange shaded region corresponds to the tail area (in m^2) comprising the entirety of the flukes and the peduncle region caudal to the cranial fluke insertions.
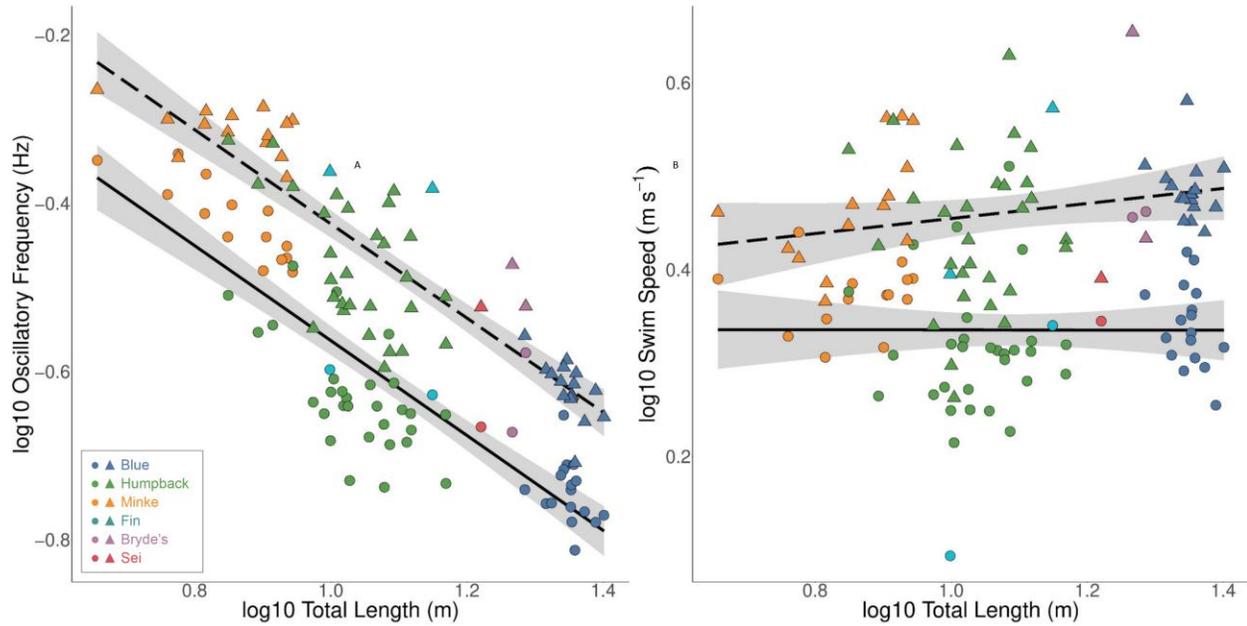
Figure 3. Linear regressions showing the $\log^{10}$ of total body length (m) versus the A) oscillatory frequency (Hz) and B) swim speed (m s^{-1}) for both routine swimming (solid line) and lunge-associated swimming (dashed line). Each point corresponds to the mean value for a single individual whale and a single swimming mode (● circle: routine; ▲ triangle: lunge-associated).
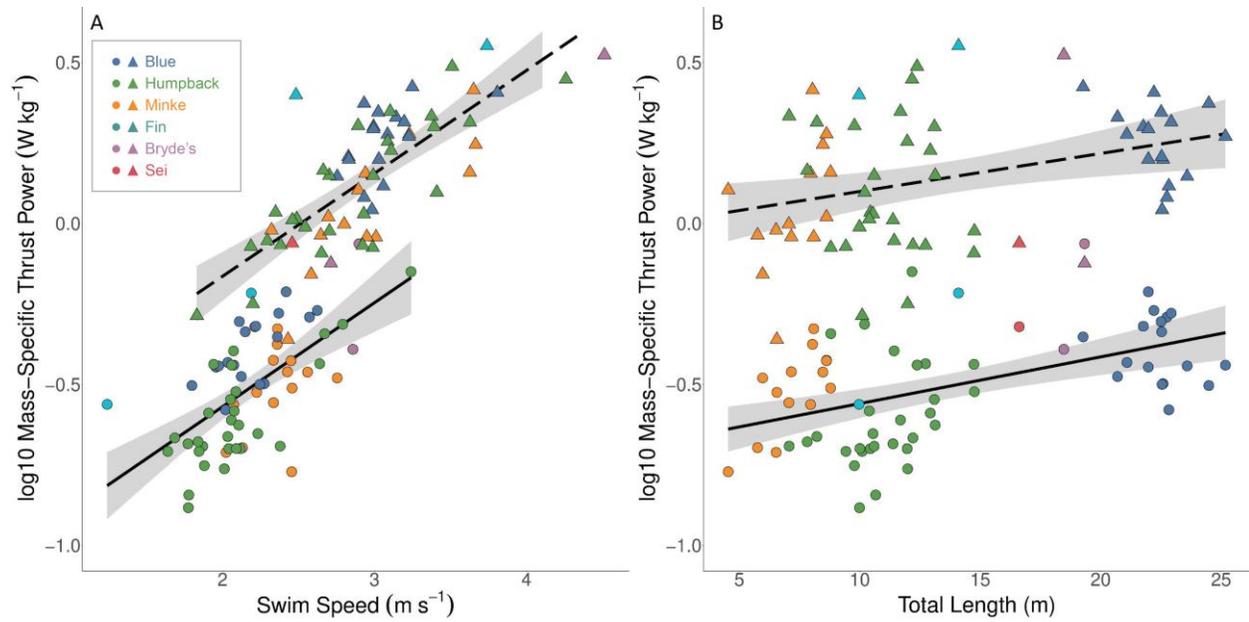
Figure 4. Linear regressions showing A) swim speed (m s^{-1}) and B) total body length (m) versus the log^{10} of mass-specific thrust power output (W kg^{-1}) for both routine swimming (solid line) and lunge-associated swimming (dashed line). Each point corresponds to the mean value for a single individual whale and a single swimming mode (● circle: routine; ▲ triangle: lunge-associated).
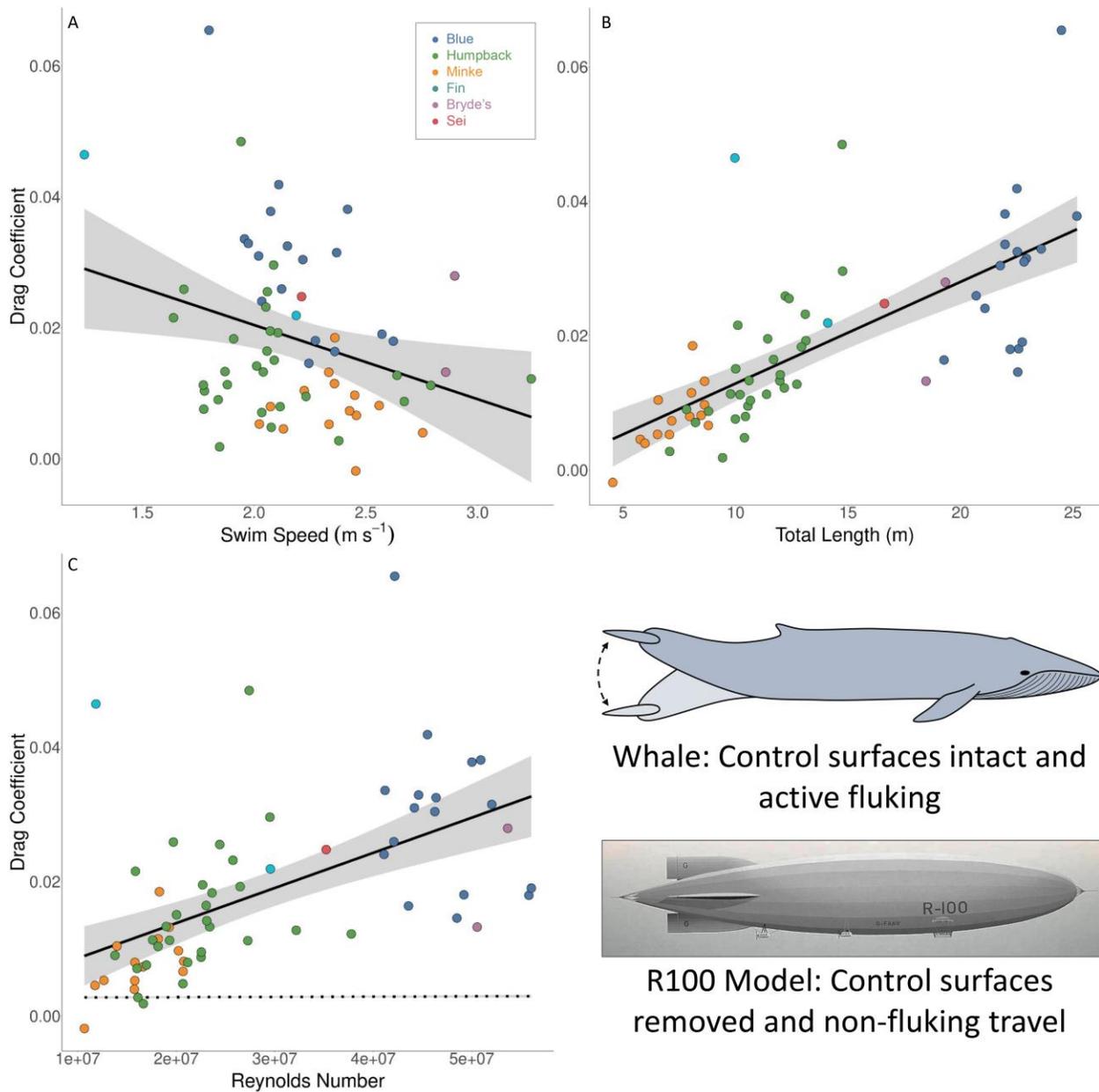
Figure 5. Linear regressions showing A) swim speed (m s^{-1}), B) total body length (m), and C) Reynolds number (dimensionless) versus the drag coefficient (dimensionless) for routine swimming (solid line). Each point corresponds to the mean value for a single individual whale and a single swimming mode (● circle: routine; ▲ triangle: lunge-associated). Dotted line shown in C) is a linear regression of Reynolds number versus drag coefficient for a simple rigid-body model comparison using equations derived from Hoerner (1965). Illustration shows a swimming blue whale and image shows an R100 rigid-body as visual representations of the data shown in C).
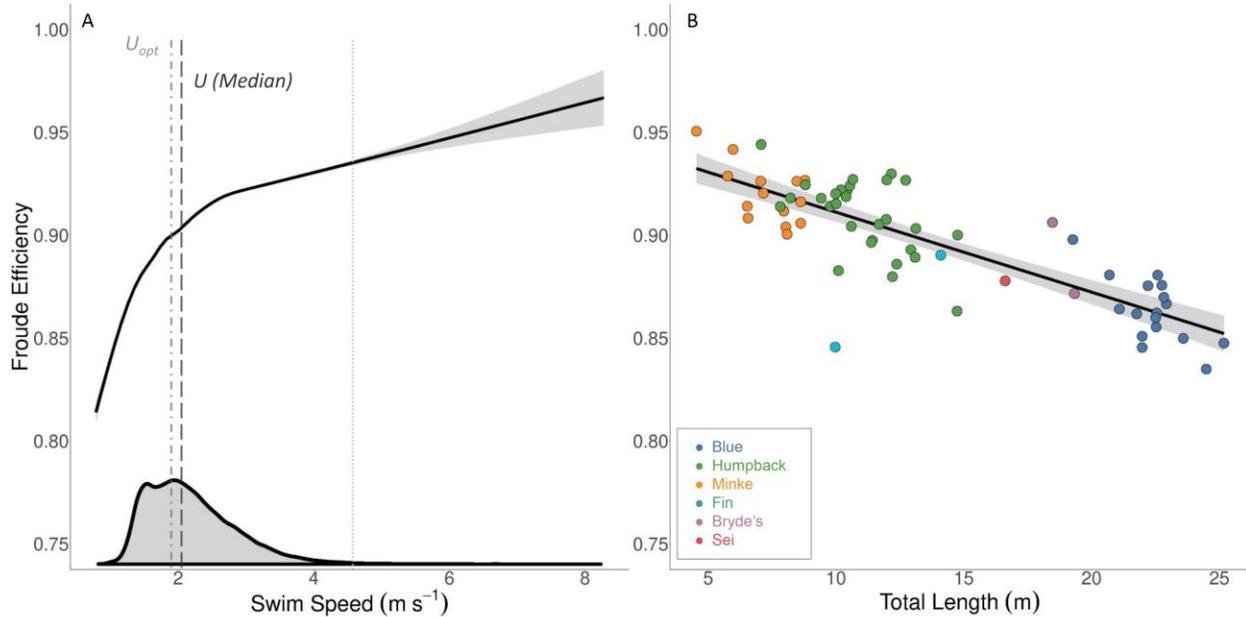
Figure 6. Curved fit lines showing A) swim speed (m s^{-1}) and linear regression showing B) total body length (m) versus Froude efficiency (dimensionless) for routine swimming (solid line). Curved fit line shown in A) is based upon each individual tailbeat measurement for all species combined and shows the plateau in Froude efficiency that occurs at 2-2.5 m s^{-1}. Vertical black dashed line in A) denotes the median routine swimming speed across all species (2.06 m s^{-1}). Vertical grey dot-dashed line in A) denotes the optimal swimming speed (U_{opt}; 1.97 m s^{-1}) calculated by Gough et al. (2019). Vertical grey dotted line at 4.5 m s^{-1} in A) denotes the 99th percentile, with only 1% of the data falling to the right of the line. Each point in B) corresponds to the mean value for a single individual whale. Grey density plot along x-axis of A) shows the density of swim speeds for all species combined.
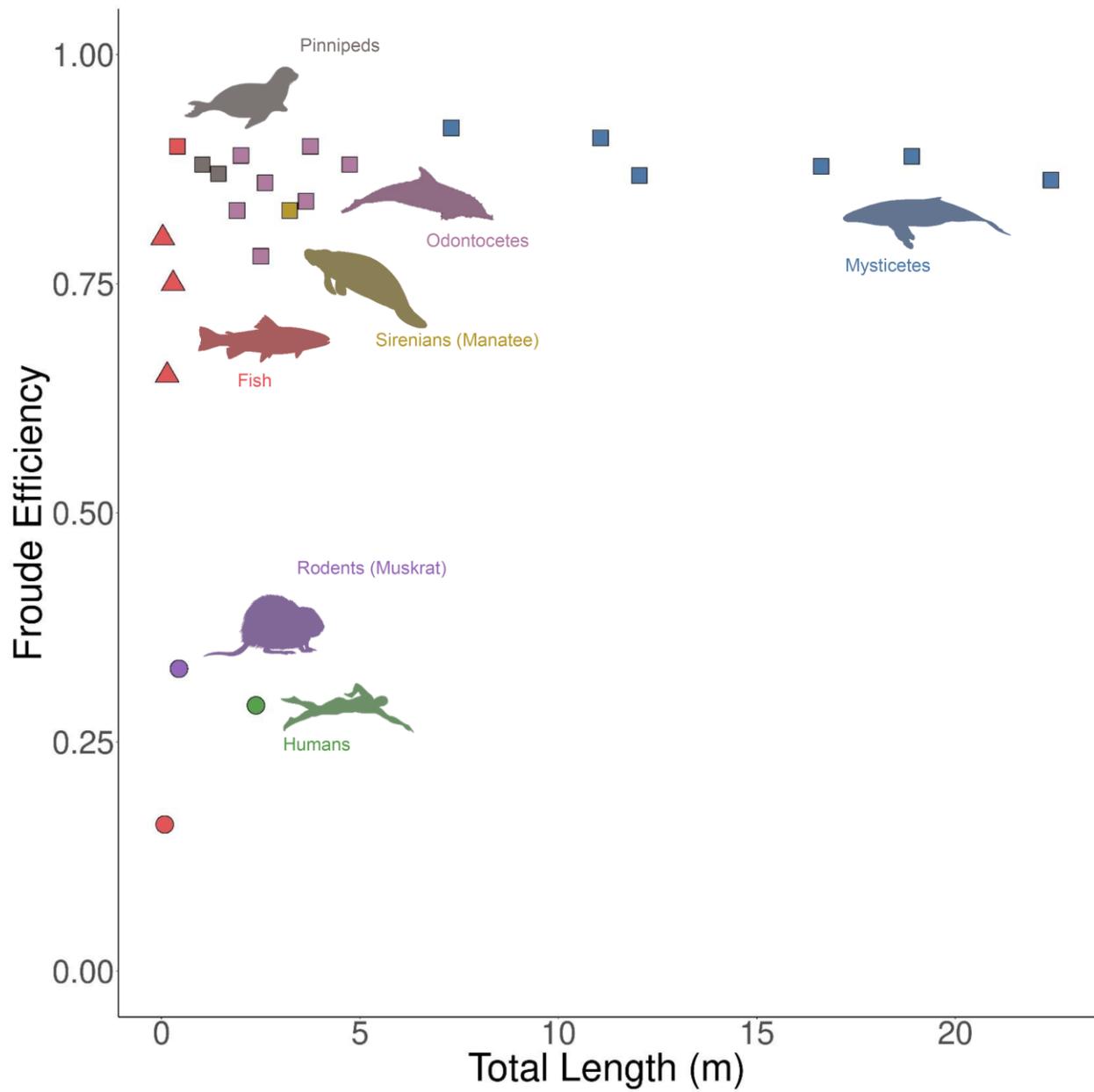
Figure 7. Froude efficiency versus total body length (m) for species from different morphological and taxonomic groups and use different swimming modes (● circle: drag-based paddling; ▲ triangle: undulatory swimming; ■ square: oscillatory swimming). The values for mysticete cetaceans are the mean species-level data from our present study. Silhouettes correspond to each group by rough position and color.

Tables

Table 1. Kinematic and morphometric variables used for modeling of hydrodynamic properties for all (n=65) individual whales in our dataset. Those with an asterisk were modeled using available data and methods in the literature. All values are given as the mean ± the standard error.

Species	Number of Individuals	Kinematics						Morphometrics				
		Swim Speed (Routine) ($m\ s^{-1}$)	ΔU (Routine) ($m\ s^{-1}$) (% of mean)	Oscillatory Frequency (Routine) (Hz)	Swim Speed (Lunge) ($m\ s^{-1}$)	ΔU (Lunge) ($m\ s^{-1}$) (% of mean)	Oscillatory Frequency (Lunge) (Hz)	Total Length (m)	Wetted Surface Area (m^2)	Body Mass (kg)	Chord Length (m)	Fluke Area (m^2)
Humpback	29	2.09 ± 0.066	0.08 ± 0.012 (11.60 ± 0.900)	0.24 ± 0.007	2.81 ± 0.100	0.46 ± 0.055 (26.68 ± 1.899)	0.34 ± 0.011	11.06 ± 0.35	61.35 ± 1.93	20470.46 ± 1458.07	1.05 ± 0.03	3.12 ± 0.19
Blue	17	2.20 ± 0.054	0.15 ± 0.027 (16.04 ± 0.875)	0.18 ± 0.004	3.06 ± 0.057	0.80 ± 0.038 (32.09 ± 1.369)	0.24 ± 0.004	22.41 ± 0.33	151.86 ± 2.23	66338.22 ± 3206.04	1.28 ± 0.03	4.67 ± 0.19
Antarctic Minke	14	2.35 ± 0.052	0.06 ± 0.009 (10.89 ± 0.473)	0.38 ± 0.011	2.96 ± 0.118	0.36 ± 0.068 (19.80 ± 1.272)	0.49 ± 0.008	7.30 ± 0.34	25.54 ± 1.21	5528.91 ± 450.57	0.55 ± 0.03	0.77 ± 0.06
Bryde's	2	1.71 ± 0.47	0.05 ± 0.028 (7.62 ± 0.153)	0.24 ± 0.008	3.11 ± 0.629	0.53 ± 0.134 (25.79 ± 5.881)	0.42 ± 0.010	12.04 ± 2.07	51.32 ± 16.39	11737.54 ± 5193.87	0.81 ± 0.13	1.97 ± 0.56
Fin	2	2.88 ± 0.020	-0.07 ± 0.030 (15.06 ± 1.256)	0.24 ± 0.026	3.61 ± 0.900	0.40 ± 0.412 (22.43 ± 0.393)	0.32 ± 0.018	18.90 ± 0.43	109.90 ± 2.50	39515.13 ± 2330.65	1.07 ± 0.07	2.78 ± 0.35
Sei	1	2.21	0.09 (9.59)	0.22	2.46	0.37 (17.33)	0.30	16.62	92.71	27275.04	1.15	3.23

Table 2. This table contains equations, estimates, R² values, and p values from generalized linear mixed models for sequential figures 3-6.

Log^{10} Oscillatory Frequency (Hz) vs. Log^{10} Total Length (m) (Figure 3)	Linear equation	R2	P – value
Routine Effort Swimming	ŷ = -0.565x + 0.003	0.75	<0.001
Lunge-Associated Swimming	ŷ = -0.560x + 0.312	0.77	<0.001

Log^{10} Swim Speed (m s^{-1}) vs. Log^{10} Total Length (m) (Figure 3)			
Routine Effort Swimming	ŷ = -0.001x + 0.774	$6.27*10^{-6}$	0.984
Lunge-Associated Swimming	ŷ = 0.080x + 0.862	0.04	0.091

Log^{10} Mean Mass-Specific Thrust Power vs. Swim Speed (m s^{-1}) (Figure 4)			
Routine Effort Swimming	ŷ = 0.381x – 1.215	0.38	< 0.001
Lunge-Associated Swimming	ŷ = 0.320x – 0.804	0.57	< 0.001

Log^{10} Mean Mass-Specific Thrust Power vs. Total Length (Figure 4)			
Routine Effort Swimming	ŷ = 0.015x – 0.705	0.24	< 0.001
Lunge-Associated Swimming	ŷ = 0.011x – 0.019	0.12	0.005

Drag Coefficient vs. Swim Speed (m s^{-1}) (Figure 5)			
Routine Effort Swimming	ŷ = -0.011x + 0.043	0.09	0.015

Drag Coefficient vs. Total Length (m) (Figure 5)			
Routine Effort Swimming	ŷ = 0.002x – 0.002	0.50	<0.001

Drag Coefficient vs. Reynolds Number *(Figure 5)*			
Routine Effort Swimming	$\hat{y} = 5.23*10^{-10}x - 3.36*10^{-3}$	0.31	<0.001
Froude Efficiency vs. Total Length (m) *(Figure 6)*			
Routine Effort Swimming	$\hat{y} = -0.004x - 0.950$	0.68	< 0.001

Table 3. Results from hydrodynamic and morphometric calculations for all individuals (n=65) from each species. All values are given as the mean of all routine tailbeats in a deployment ± the standard error. For mass-specific thrust power, we have included the mean of all lunge-associated tailbeats in a deployment ± the standard error. The drag coefficient, Reynolds number, and Froude efficiency are dimensionless.

	Hydrodynamic Calculations			
Species	***Mass-Specific Thrust Power (Watts kg^{-1})***	***Drag Coefficient***	***Reynolds Number***	***Froude Efficiency***
Humpback	0.27 ± 0.023 (1.30 ± 0.138)	0.015 ± 0.001	2.22 x 10^7 ± 1.0 x 10^6	0.909 ± 0.003
Blue	0.42 ± 0.024 (1.85 ± 0.111)	0.030 ± 0.003	4.70 x 10^7 ± 1.2 x 10^6	0.863 ± 0.004
Antarctic Minke	0.31 ± 0.023 (1.23 ± 0.150)	0.008 ± 0.001	1.65 x 10^7 ± 8.8 x 10^5	0.920 ± 0.004

Bryde's	0.44 ± 0.167 (3.03 ± 0.527)	0.034 ± 0.012	2.07×10^7 ± 8.9×10^6	0.868 ± 0.022
Fin	0.64 ± 0.229 (2.04 ± 1.293)	0.021 ± 0.007	5.21×10^7 ± 1.5×10^6	0.889 ± 0.018
Sei	0.48 (0.87)	0.025	3.52×10^7	0.878

Table S1. All symbols and corresponding definitions (with units) used throughout the manuscript. Symbols are presented in the order in which they appear in the text.

Symbol	Definition
GSD	Ground sampling distance (m)
L_{body}	Body length (m)
n_{pix}	Number of pixels (count)
a	Altitude (m)
l_{foc}	Focal length (mm)
S_w	Sensor width (mm)
P_w	Image resolution width (px)
F_a	Planar fluke area (m^2)
C	Chord length of tail (m)
M_{body}	Body mass (kg)
S_a	Wetted surface area of body (m^2)
U_{avg}	Mean swimming velocity (m s^{-1})
f	Oscillatory frequency (Hz)
T_{beat}	Duration of a tailbeat (s)
$\bar{P}_T$	Mechanical thrust power (W)
C_D	Coefficient of drag (dimensionless)
η	Froude efficiency (dimensionless)
σ	Reduced frequency (dimensionless)
ω	Angular frequency of fluking (Hz)
θ	Feathering parameter (dimensionless)
α	Angle of attack of flukes (degrees)
h	Heaving amplitude (m)
C_T	Coefficient of thrust (dimensionless)
$\bar{T}$	Mean thrust force (N)
ρ	Density of seawater (Kg m^{-3})
$\bar{D}$	Mean drag force (N)
$\bar{a}$	Mean acceleration (m s^{-2})
U_f	Final tailbeat swimming speed (m s^{-1})
U_i	Initial tailbeat swimming speed (m s^{-1})
ΔU	Change in tailbeat swimming speed (m s^{-1})
k_{added}	Shape drag correction factor (dimensionless)
$C_D^{routine}$	Mean drag coefficient for all routine tailbeats from a single whale (dimensionless)
$\bar{P}_T^{lunge}$	Thrust power for a lunge-associated tailbeat (W)
C_D^{mod}	Drag coefficient from rigid airship model
W_{max}	Maximum body diameter (m)
Re	Reynold's number (dimensionless)

Table S2. Equations used to calculate the wetted surface area of each species as well as literature sources.

Species	Source	Body Length (m)	Surface Area (m²)	Surface Area Equation
Humpback	CFD model – Kennedy (2021)	14.78	82	$S_a = 5.55 \times L_{body}$
Blue	Kermack, 1948	25.91	175.59	$S_a = 6.78 \times L_{body}$
Antarctic Minke	CFD model – Kennedy (2021)	8	28	$S_a = 3.50 \times L_{body}$
Bryde's	Fish (pers comm.)	-	-	$S_a = 0.43185 \times L_{body}^{1.9103}$
Fin	Parry, 1949	19.8	137	$S_a = 5.81 \times L_{body}$
	Kermack, 1948	20.12	115.11	
	Kermack, 1948	21.1	126.07	
	Bose and Lien, 1989	14.5	67.35	
Sei	Fish (pers comm.)	-	-	$S_a = 0.43185 \times L_{body}^{1.9103}$

Table S3. Froude efficiency and metadata collected from various sources for the creation of figure 7.

Species	Swim Speed (m s^{-1}) or (bl s^{-1})*	Total Length (m)	Froude Efficiency	Source(s)
Homo sapien *Human (Female)*	0.95	2.38	0.29	von Loebbecke et al., 2009
Ondatra zibethicus *Muskrat*	0.75	0.44	0.33	Fish, 1984
Pterophyllum eimekei *Freshwater Angelfish*	0.04	0.08	0.16	Blake, 1979; Blake, 1980
Danio rerio *Zebra Danio*	Multiple	0.0315	0.80	McCutchen, 1975
Cymatogaster aggregata *Shiner Perch*	0.57	0.143	0.65	Webb, 1975
Oncorhynchus mykiss *Rainbow Trout*	U_{crit}	0.293	0.75	Webb, 1975
Euthynnus affinis *Mackerel Tuna (Kawakawa)*	1.52	0.40	0.90	Magnuson, 1978
Pusa hispida *Ringed Seal*	0.75	1.03	0.88	Fish et al., 1988
Pagophilus groenlandicus *Harp Seal*	1.04	1.43	0.87	Fish et al., 1988
Trichechus manatus *American Manatee*	0.30*	3.23	0.83	Kojeszewski and Fish, 2007
Delphinapterus leucas *Beluga Whale*	3.00	3.64	0.84	Fish 1998
Lagenorhynchus obliquidens *Pacific White-Sided Dolphin*	5.30	2.00	0.89	Webb, 1975; Yates, 1983; Blickhan and Cheng, 1994

Orcinus orca *Killer Whale*	6.50	4.74	0.88	Fish, 1998
Pseudorca crassidens *False Killer Whale*	3.80	3.75	0.90	Fish, 1998
Sotalia guianensis *Guiana Dolphin*	2.40	1.90	0.83	Blickhan and Cheng, 1994
Tursiops truncatus *Common Bottlenose Dolphin*	2.40[1], 3.80[2]	2.50[1], 2.61[2]	0.78[1], 0.86[2]	Blickhan and Cheng, 1994[1]; Fish, 1998[2]
Megaptera Novaeangliae *Humpback Whale*	2.09 ± 0.066 (Routine Effort Swimming)	11.06 ± 0.35	0.909 ± 0.003	Current Study
Balaenoptera musculus *Blue Whale*	2.20 ± 0.054 (Routine Effort Swimming)	22.41 ± 0.33	0.863 ± 0.004	Current Study
Balaenoptera bonaerensis *Antarctic Minke Whale*	2.35 ± 0.052 (Routine Effort Swimming)	7.30 ± 0.34	0.920 ± 0.004	Current Study
Balaenoptera brydei *Bryde's Whale*	1.71 ± 0.47 (Routine Effort Swimming)	12.04 ± 2.07	0.868 ± 0.022	Current Study
Balaenoptera physalus *Fin Whale*	2.88 ± 0.020 (Routine Effort Swimming)	18.90 ± 0.43	0.889 ± 0.018	Current Study
Balaenoptera borealis *Sei Whale*	2.21 (Routine Effort Swimming)	16.62	0.878	Current Study